The use of Rayleigh-wave ellipticity for site-specific hazard assessment and microzonation: application to the city of Lucerne, Switzerland

Valerio Poggi, Donat Fäh, Jan Burjanek and Domenico Giardini

Swiss Seismological Service, Institute of Geophysics, ETH Zürich, Zürich, Switzerland. E-mail: poggi@sed.ethz.ch

SUMMARY

The sediments underlying the city of Lucerne (Switzerland) consisting of fluvio-lacustrine deposits of Quaternary age have the potential to produce strong amplification of the seismic wavefield. To obtain a reliable estimation of the deep soil structure, we combine different methodologies based on ambient noise recordings, such as single station horizontal to vertical ratios and three-component array analysis. Two novel techniques to estimate Rayleigh-wave ellipticity from ambient noise recordings are tested. These are based on a single- and a multistation approach, respectively. The first utilizes the continuous wavelet transform to perform a decomposition of the noise wavefield and to isolate and extract the Rayleigh-wave contribution. The second, conversely, relies on a high-resolution f–k method to achieve the same result. We compare the results from the two techniques to provide an evaluation of their capabilities and limitations. A two-step inversion scheme is then presented to improve resolution on the bedrock depth. In particular, the surface wave dispersion information is initially used to constrain the soft sediment part, while the Rayleigh-wave ellipticity peak is subsequently used for constraining the bedrock depth. It is shown that such an approach is beneficial to map the bedrock geometry over dense urban areas. The output velocity model is then used to compute the local seismic amplification by means of gridded 1-D approximation.

Key words: Wavelet transform; Surface waves and free oscillations; Site effects.

1 INTRODUCTION

Calculation of the (deterministic) amplification factors is based on an accurate knowledge of the elastic properties of the constituting materials down to a sufficient depth, preferably into the bedrock. High costs of implementation and the difficulty in reaching larger depths, however, make direct investigation not always sustainable for engineering site–response analysis. The alternative use of geophysical techniques can lead to reliable results over wide areas and large depths, with a comparatively lower effort. Among those, techniques based on ambient vibration are of special interest (e.g. Arai & Tokimatsu 2005; Asten *et al.* 2005; Bard *et al.* 2005). Even if passive methods provide coarser results with respect to other geophysical approaches, they have the advantage of being cheap and easy to implement, which makes them suitable for most engineering purposes. They are also suitable in densely populated areas, which is often the case in microzonation studies.

In this paper, a strategy is presented for evaluating the local seismic response of 3-D sedimentary basins using ambient noise techniques. In particular, we propose the use of Rayleigh-wave ellipticity information to obtain a simple but reliable assessment of the bedrock depth. The method basically consists of the separate assessment of the velocity structure of the sediment and the bedrock

depth. The method is similar to what has been proposed by Arai & Tokimatsu (2008). In a first stage, a generic velocity profile (in terms of P and S velocities) is established for the soft-sediment part from the surface wave dispersion and polarization characteristics resulting from the analysis of noise array data. Subsequently, the Rayleigh-wave ellipticity peak from single station measurements is used to resolve the geophysical bedrock depth. Two new methodologies to retrieve the Rayleigh-wave ellipticity information from ambient vibration are tested. A first approach is the one proposed by Poggi & Fäh (2010), based on a modification of the high-resolution method of Capon (1969) to estimate the Rayleigh particle motion from three-component array recordings of ambient noise. The second approach (Fäh *et al.* 2009), developed during the NERIES project (NEtwork of Research Infrastructures for European Seismology, JRA4 'Geotechnical Site Characterization'), uses the wavelet time–frequency analysis of single station recordings to achieve the same goal. Both methods present some advantages and disadvantages. It is the target of this paper to compare capabilities and limitations of such techniques, and to show how their combined use can provide important information for the characterization of the seismic response of a site.

From historical and instrumental evidences, the city of Lucerne (Switzerland) is prone to low-to-moderate seismicity, with a chance
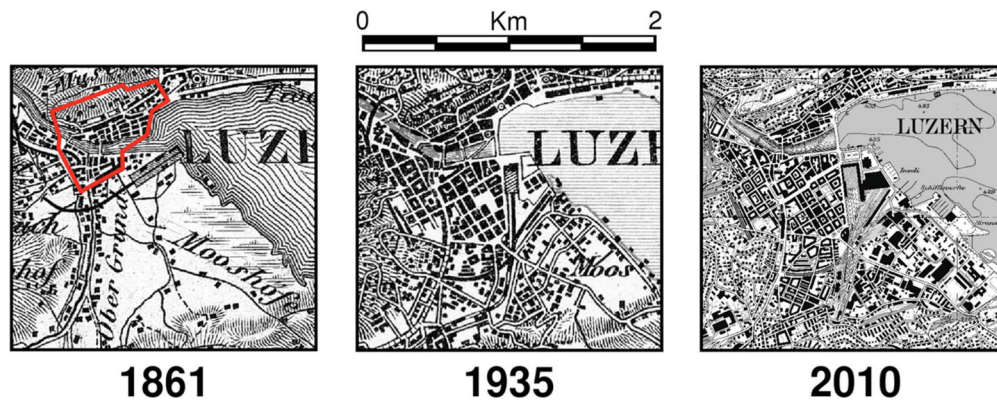
Figure 1. Historical evolution of the city of Lucerne from 1861 up today. The red line indicates the possible borders of the old settlement in the 16th century.

of very strong earthquakes over long return periods. Risk mitigation measures are therefore important to undertake. Target of this study is the characterization of the local seismic response of the Lucerne sedimentary basin by means of ambient vibration techniques. The velocity structure obtained from the analysis of single station and array recordings of ambient noise is used as a model for the entire sediment cover. For simplification, local variability of velocity and possible non-linear effects in the shallower parts of the profile are here not considered. The retrieved velocity model is then used as input to model the seismic amplification response of the study area. Due to the level of uncertainty in the surface part of the input model, however, a simplified pseudo-3-D approach has been preferred, where the 3-D amplification model is approximated by a horizontal grid of a large number of 1-D *SH*-wave transfer functions for vertical propagation.

2 GEOLOGICAL SETTING

The sedimentary basin underlying the city of Lucerne (Switzerland) consists of an alternation of fluvio-lacustine deposits of Quaternary age. Thick sand layers are alternated with coarse gravels and fine-layered deposits (mostly silt and clay). Alluvial fans had a major influence in the structure of the outer basin, where the material is generally coarser and large-grained. Outside the basin edges, the basement bedrock is largely exposed. It consists of a mixture of clastic sedimentary materials, which originated through sin-orogenic accretion during the Alpine evolution (the subalpine Molasse basin). The bedrock interface geometry, as well as the surface morphology, is the heritage of an alternation of successive inter- and intraglacial events.

From the geotechnical point of view, the basin area has been defined by previous investigations (Mengis & Lorenz AG 2007, unpublished data) predominantly as category D and C, or F1 of the Swiss Building Code classification (SIA261 – action on structures 2003). The soil classes are fairly comparable to the classification in EC8 (CEN 2004), however with some slight difference in the *S*-wave velocity bounds. From borehole measurements, the first ground water table has been found to be generally shallow, often at less than 5 m in depth, depending on the proximity to the lake and the topographic elevation.

3 HISTORICAL SEISMICITY OF THE STUDY AREA

Moderate seismicity of central Switzerland can be characterized by the irregular episodes of stronger earthquakes, both in space and time (Gisler *et al.* 2004). Earthquake activity has been very low since the beginning of modern instrumental observations in the 1970s. The largest known earthquakes in the past are the 1601 September 18 (M_w 5.9), the 1774 September 10 (M_w 5.7) and the earthquake swarms of 1777 and 1964. The epicentres of these events indicate a concentration of activity around Altdorf (1774, 1775) and Sarnen (1601, 1777, 1964), whereas recent instrumentally observed earthquakes are distributed uniformly over the whole area. Moreover, three large palaeo-earthquakes were identified in central Switzerland with moment magnitudes (M_w 6.5–7.0), significantly exceeding historically known values (Strasser *et al.* 2006).

The 1601 earthquake is the strongest historical event in central Switzerland of the past millennium and among the seven strongest events in Switzerland known from historical sources (Schwarz-Zanetti *et al.* 2003). The main shock of September 18 with $M_w = 5.9$ produced rockfalls at many places in central Switzerland. However, only those on Mt Hahnen near Engelberg and Mt Bürgenstock are described in detail by historical sources. Rockfall at Bürgenstock into the Lake Lucerne and the earthquake triggering of a subaquatic landslide caused a tsunami and a seiche. The seiche caused the river Reuss in Lucerne to flow back six times during the first hour after the earthquake, with the result that each time the riverbed was empty for several minutes (Schwarz-Zanetti *et al.* 2003). Chimneys and tiles fell and walls cracked in the whole of Lucerne. However, most seriously affected was the so-called 'little town', in particular the towers of the city wall. Only a small part of the marshland was developed at the time of the historical earthquakes. Urbanization started at the end of the 19th and beginning of the 20th century. Today, buildings and infrastructure cover the whole area (Fig. 1). Together with the evidence of a dense population of the area, a seismic characterization of the Lucerne City is of primary importance. Adequate risk mitigation measures have to be undertaken (Basler & Partner 2007). This work mainly focuses on the seismic characterization of the 'little town' area.

4 AMBIENT NOISE MEASUREMENTS

4.1 General set-up and single station measurements

To reconstruct the seismic velocity structure of the basin of Lucerne, an extensive ambient noise survey was performed, consisting of 101 single station measurements and some large-aperture array deployments (Fig. 2). All the measurements were conducted with seismological equipment, consisting of 24 bit data loggers (Quanterra Q330) and three-component velocity sensors with 5 s eigenperiod (Lennartz LE3d/5s).
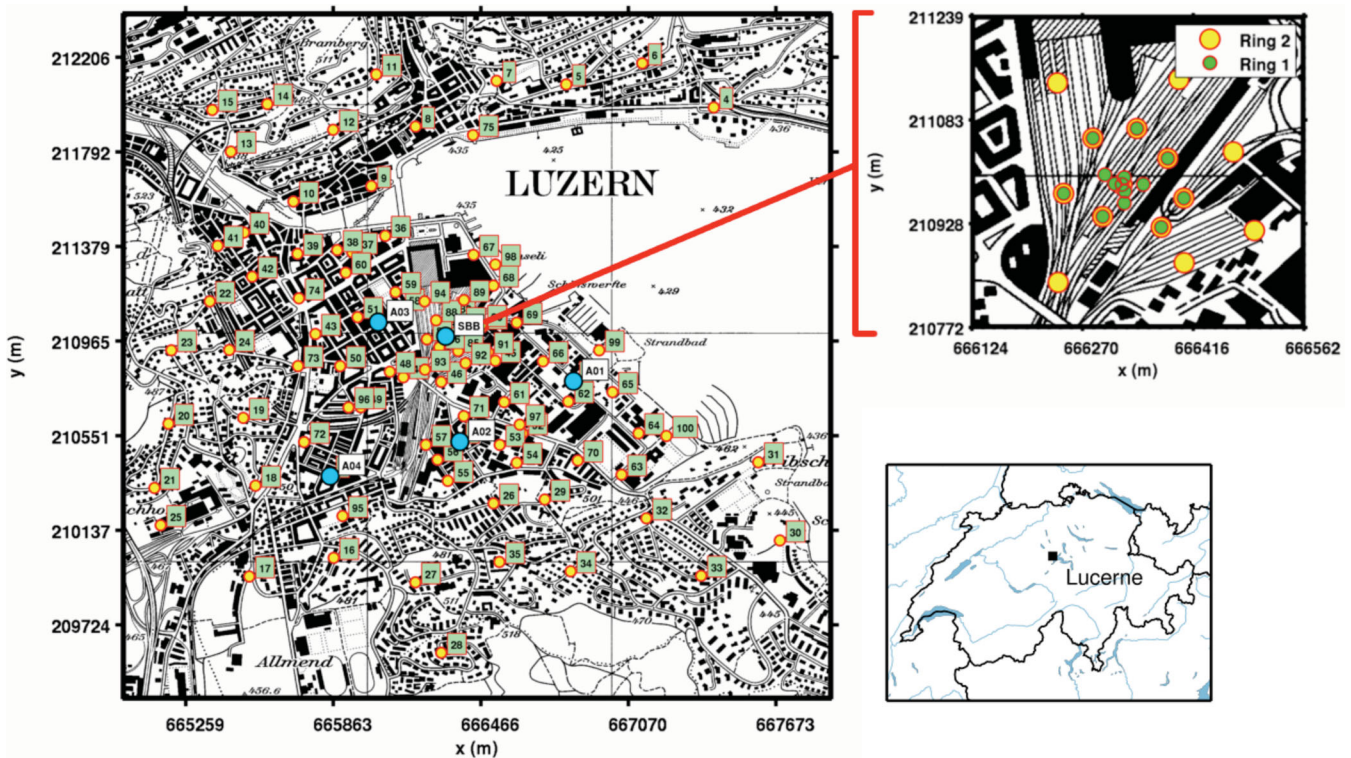
Figure 2. Ambient noise measurements performed in the city of Lucerne (Switzerland). On the left-hand side, the map of the 101 single station measurement locations (yellow dots) and five array measurements (blue dots). On the top-right panel, particular of the large-aperture array deployment within the main train station (SBB array). Units are in Swiss Coordinates (CH1903+).

For single station measurements, noise was recorded for a duration varying between 20 and 40 min, depending on the level of urban disturbances. The measurement survey was set-up in two separate stages. In a first round about 60 sites were investigated within the innermost area of the basin to characterize Quaternary sediments underlying the city. While in a second stage, the remaining measurements were performed to refine the contact between soft sediments and outcropping bedrock at the basin edge.

4.2 The array survey

Five arrays of different sizes were deployed within the Lucerne basin to investigate the velocity structure of the sediments beneath the urban area. The largest array deployment was set up in the innermost part of the basin (Fig. 2), using the area of the Swiss Federal Railways (SBB) main station (SBB array hereinafter). The widest possible receiver configuration was decided (about 350 m in diameter), to maximize the resolving power at depth. In general, the exact depth resolution cannot be determined *a priori*, as it is controlled, apart from the array size, by the elastic properties of the subsurface material and the signal-to-noise ratio in the frequency range of interest (e.g. Jongmans *et al.* 2005). Several empirical relations have been proposed in the literature (e.g. Tokimatsu 1997; Okada 2003), which are nevertheless reliable only as first approximation. Based on our prior knowledge, we estimated therefore a maximum resolving depth for the SBB array of about 100~150 m. Measurements were conducted overnight and train traffic was stopped during the recording periods (approximately 2 hr). The installation consisted of two concentric rings of increasing diameter and 14 receivers each. The first ring (smaller and internal) had a diameter of about 200 m, while the second had a diameter of about 350 m. Since the array methods rely on the phase-delay estimation, it is necessary to

accurately assess the relative station location, to correctly process the data. Generally, the location error should not be higher than 1–2 per cent of the total array radius (Jongmans *et al.* 2005). To achieve such accuracy in the station location, a telemetric survey was performed using a laser theodolite.

Four arrays (named 01, 02, 03 and 04) were additionally installed in the surrounding areas of the SBB array, with the aim of mapping any lateral variation of seismic velocities in the uppermost layers. However, the recordings of these arrays were biased by the high level of urban disturbances. In particular, array 03 failed completely while array 01 provided consistent results over a limited frequency band. Consequently, we rely mostly on the results of the SBB array for the evaluation of a characteristic soil profile for the basin.

4.3 Error estimation in orienting the horizontal components

For the elaboration of three-component recordings, special attention has to be paid to the correct alignment of the sensors. An external reference is required for the horizontal components, common to all stations. Usually the magnetic North is used, detected by compass. In the case of the SBB array, however, the detection of the magnetic North direction was limited by the presence of ferromagnetic material (e.g. rail lines and wagons) and electric power lines within the station. We implemented a quality control procedure on the recordings to assess the sensor orientation. It is based on two assumptions: (1) the very low-frequency content of the recorded motion (below fundamental frequency of the site) is nearly in phase across the array; (2) at least one station of the array is known to be precisely oriented (the reference station). Recordings of the two horizontal components were bandpass filtered between 0.5 and 1 Hz, as we deal with the 5 s sensor, and the fundamental frequency
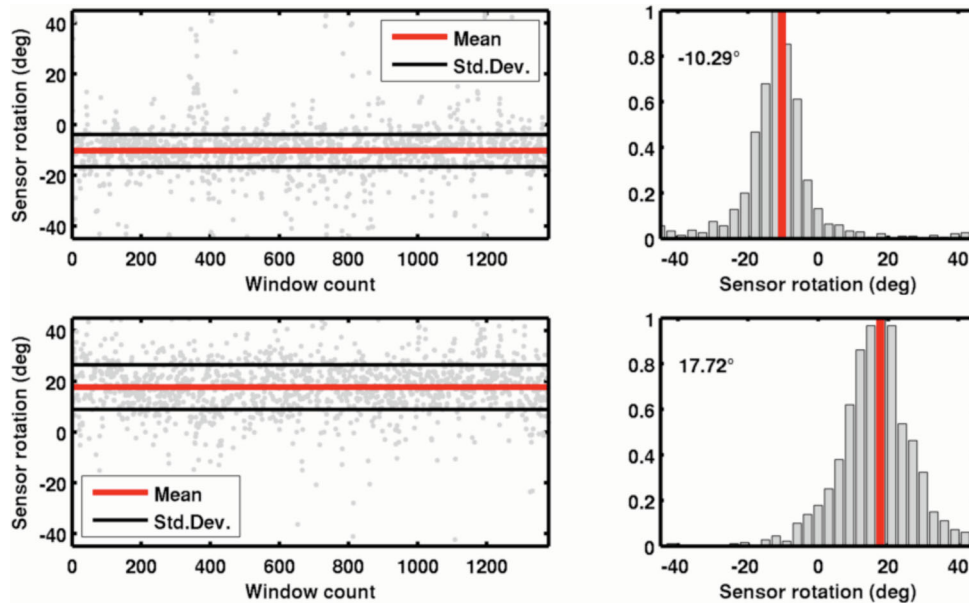
Figure 3. Two examples of the orientation error on the horizontal components of a sensor due to the use of a compass. The analysis is relative to a base station (central station of array SBB) aligned to North. The total error between stations can be quite high, for example, about 27° in this example.

of the site is above 1 Hz. The recordings are subsequently divided in 50 per cent overlapping windows of equal length (around 10 s), progressively rotated over different azimuths, and compared with recordings of the reference station using the L2 norm. The central one was used as the reference station in this case. Finally, the azimuths corresponding to maximum correlation are collected for all windows, and statistical analysis is performed by means of histograms. For the SBB array, large discrepancies were found in the sensor alignment, with deviation up to 27° in total (e.g. Fig. 3). An error of such magnitude, if not corrected, would produce considerable deviations in the results of the three-component f–k analysis.

5 SINGLE STATION PROCESSING

5.1 Classical *H/V* ratios

The horizontal-to-vertical Fourier spectral ratio is a technique widely used in seismic site characterization (see Bonnefoy-Claudet *et al.* 2006b for an exhaustive reference list). It has been applied to earthquake signals (e.g. Chavez-Garcia *et al.* 1996; Lachet *et al.* 1996; Theodulidis *et al.* 1996), but nowadays the most common application is with ambient noise recordings. The major advantage of the method is its capability to give a reliable estimate of the *SH* waves fundamental frequency of resonance (f_0) of a site (e.g. Haghshenas *et al.* 2008 and references therein) without the need to wait for earthquakes. Following the explanation proposed by Nakamura (1989) the shape of *H/V* spectra should be controlled by the effect of *SH* waves resonating along the structure. Nevertheless, it has been experimentally demonstrated that the shape and the amplitude of the *H/V* spectral ratio is generally not representative of the site *SH*-wave transfer function, but only the fundamental frequency is correctly retrieved from it (e.g. Haghshenas *et al.* 2008). On the other hand, it has been shown, that the shape of the *H/V* ratio is rather linked to the Rayleigh-wave ellipticity curve (e.g. Lermo & Chavez-Garcıa 1994; Fäh *et al.* 2001, 2003; Malischewsky & Scherbaum 2004).

Let us briefly discuss the content of ambient vibration wavefield, which is the key to understanding the shape of the *H/V* spectral

ratio. Unfortunately the problem is non-trivial, depending on the velocity structure and the characteristics of the noise sources. In the presence of shallow sources and a strong velocity contrast between sediments and bedrock, surface waves dominate in the ambient vibration wavefield at frequencies above f_0 (e.g. Horike 1985). Such situation reverses below f_0, where it is realistic to assume a progressive decrease in surface waves with respect to body waves (Scherbaum *et al.* 2003; Bonnefoy-Claudet *et al.* 2006a). Among surface waves, fundamental mode Rayleigh waves seem to have a major role in controlling the shape of *H/V* spectral ratios above f_0 (e.g. Fäh *et al.* 2001, 2003). In other words, *H/V* ratio is close to the fundamental mode Rayleigh-wave ellipticity curve. Nevertheless, in some cases the Love-wave contribution might still be significant (Bonnefoy-Claudet *et al.* 2008). Among body waves, however, defining the relative proportion of the *P* to *S* component still represents a major issue to be clarified (e.g. Bonnefoy-Claudet *et al.* 2006b; Endrun 2010).

Even in case of predominance of Rayleigh waves in the wavefield, *H/V* ratios cannot be directly treaded as Rayleigh ellipticity, if some correction is not applied. A common practice consists in assuming equal contribution of Love and Rayleigh waves on the horizontal plane (e.g. Fäh *et al.* 2001). Therefore, if the NS and EW horizontal components are combined using vector sum, the correction factor is a normalization by square root of two (that is equivalent to applying the quadratic mean on the components). This approximation is acceptable in most cases, but when *SH* influence becomes relevant in some frequency band, it can overestimate the Rayleigh-wave ellipticity amplitudes (Fäh *et al.* 2008).

5.2 *H/V* ratios using the continuous wavelet transform

With the aim to minimize the effect of *SH* waves, Fäh *et al.* (2001) proposed the calculation of *H/V* spectral ratios by means of time–frequency analysis. A similar but more sophisticated method, originally proposed by Kristekova (2006), was subsequently developed during the NERIES project (Fäh *et al.* 2009, NERIES JRA4, B2-D4 report). This method basically implements a continuous wavelet transform to produce an accurate time–frequency
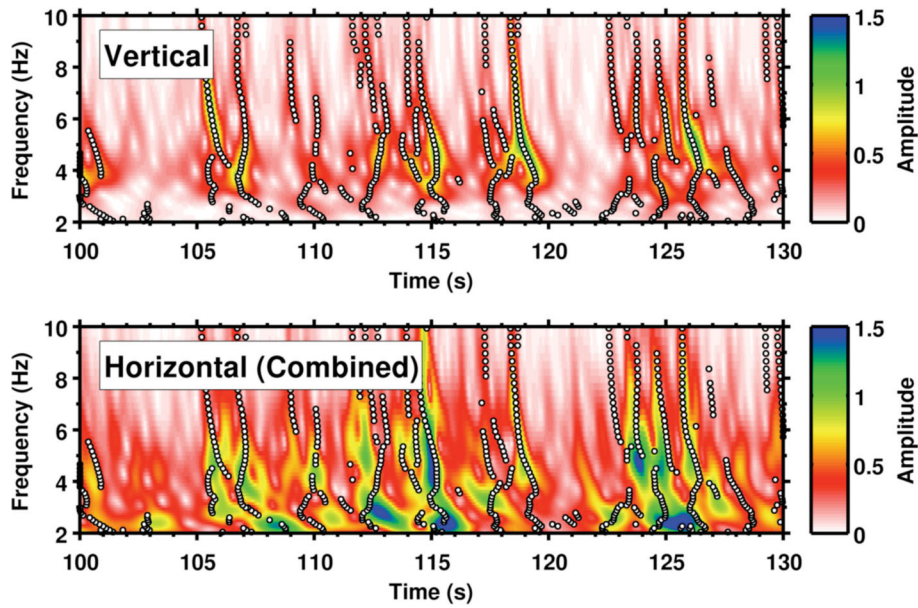
Figure 4. Example of wavefield decomposition of 30 s of noise recording using the continuous wavelet transforms. *P-SV* wavelets are isolated (white dots) on the spectrogram of the vertical component (top panel); the corresponding amplitudes are then also extracted from the vector combination of the horizontal components (bottom panel). Finally, the *H/V* ratio is performed for each picked signal.

representation of the noise signal. The three components of motion are evaluated separately; horizontal components are then combined using vector summation. The Morlet wavelet, a complex exponential modulated by a Gaussian envelope, is used as the mother wavelet (Goupillaud *et al.* 1984), due to its well-defined central frequency and the possibility to extract phase information.

The technique is based on the evidence that the vertical component is free from *SH* propagation phenomena (both body and surface waves) in laterally homogeneous structures. Moreover, *SH* and *P-SV* contributions are not expected to be synchronous on the horizontal component. Therefore, once a transient signal is identified on the vertical component of motion (through a maximum in the time–frequency amplitude spectrum, e.g. Fig. 4, top panel), the time-corresponding amplitude is extracted from the horizontal component (Fig. 4, bottom panel) and the *H/V* ratio calculated (e.g. Fig. 5). The more accurate is the time–frequency analysis, the higher is the chance to reconstruct *P-SV* particle motion. By selecting the most energetic maxima on the spectrogram, and assuming a relative minor influence of the body waves in the wavefield, retrieved *H/V* ratios represent solely the Rayleigh-wave ellipticity function. However, the method does not separate the contributions of higher modes. Therefore, in presence of strongly energetic higher modes in the wavefield, the resulting *H/V* ratio is not representative of the Rayleigh-wave fundamental mode ellipticity. In most cases, however, the energy of the fundamental mode strongly dominates.

Averaging over long time-series statistically increases the robustness of the result. The noise spectrogram is divided in several time windows of 1 min length. A simple short time-average over long time-average (STA/LTA) algorithm is used to get rid of undesired strong transient signals, due to, for example, close sources. For each window, then, all the *P-SV* signals identified on the vertical component are sorted, but only the *n* most energetic extracted. The choice of number of amplitude maxima clearly affects the result. Too few data points produce a statistically
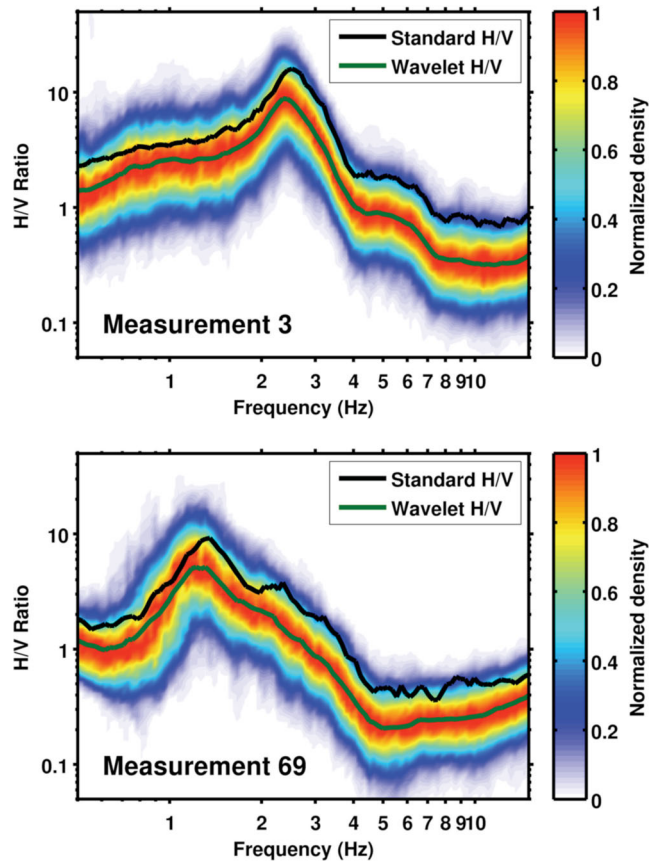

Figure 5. Comparison of *H/V* spectral ratios from the standard (in black) and the wavelet-based approaches (in green) at two station locations in Lucerne. For the wavelet analysis, a Morlet coefficient of 10 is used. Statistic is computed over about 30 min recordings, with 10 maxima/min averaging.

inconsistent result, while an excessive amount forces the inclusion of low-energy *P-SV* pulses, which might be affected by body-wave contributions. Also the choice of the mother wavelet is critical in this sense, due to the well-known trade-off between time and frequency resolution in the wavelet transform. The time–frequency resolution of the Morlet wavelet is adjusted by the wavelet parameter ω_0 (or non-dimensional central frequency), which controls the width of the Gaussian envelope. Small wavelet parameters (<6) provide an excellent time localization of the *P-SV* signals, but with an insufficient frequency resolution; conversely, a too large wavelet parameter (>50) avoids the full separation of the different wave contributions on the horizontal component. As upper bound of possibility, a wavelet coefficient equal to infinity is equivalent to performing the simple Fourier transform, thus as to using standard *H/V* ratios. For the Lucerne case, we end up with values, which we evaluate as optimal, of 10 maxima per minute and a wavelet parameter of 10.

5.3 Comparison between methods

Because of the minimization of the *SH* contribution on the horizontal components, *H/V* curves obtained with the wavelet technique are generally shifted to lower amplitude values with respect to classical *H/V* ratios (e.g. Fig. 5). In general, this amplitude decrease is frequency dependent, since the *SH* contribution may not be constant. By comparing amplitudes of *H/V* spectral ratios from the wavelet analysis and standard analysis, it is possible to roughly estimate the relative proportion of *SH* waves over frequency. If the *PSV* and *SH* sources are uniformly distributed around the measurement point, *H/V* ratios from the two methods can be expressed as follows:

$$\left(\frac{H}{V}\right)_{\text{Classic}} = \frac{\sqrt{H_{PSV}^2 + H_{SH}^2}}{V_{PSV}} \text{ and}$$
$$\left(\frac{H}{V}\right)_{\text{Wavelet}} = \frac{H_{PSV}}{V_{PSV}}. \tag{1}$$

Consequently, the *SH* contribution relative to *PSV* (horizontal and vertical) can be written as

$$\frac{H_{SH}}{H_{PSV}} = \sqrt{\frac{\left(\frac{H}{V}\right)_{\text{Classic}}^2}{\left(\frac{H}{V}\right)_{\text{Wavelet}}^2} - 1}, \tag{2}$$

$$\frac{H_{SH}}{V_{PSV}} = \sqrt{\left(\frac{H}{V}\right)_{\text{Classic}}^2 - \left(\frac{H}{V}\right)_{\text{Wavelet}}^2}. \tag{3}$$

The total *SH* to Rayleigh contribution is then expressed as follows:

$$\frac{H_{SH}}{\sqrt{H_{PSV}^2 + V_{PSV}^2}} = \frac{1}{\sqrt{\left(\frac{H_{SH}}{H_{PSV}}\right)^{-2} + \left(\frac{H_{SH}}{V_{PSV}}\right)^{-2}}}. \tag{4}$$

Additionally, if we assume pure surface wave propagation in the noise wavefield, these equations can be used to approximate the relative energy contribution between Rayleigh and Love waves.

5.4 Assessing the *SH*-wave contribution of the Lucerne area

The methodology proposed has been applied to evaluate the relative contribution of *SH* and *P-SV* components in the Lucerne basin area. All single station measurements were processed by the classical and wavelet analysis to compute *H/V* spectral ratios (e.g. Fig. 5). Because of the different bedrock depth, every measurement point is characterized by a different fundamental frequency (f_0). Consequently, the frequency range of each computation has been normalized by the site fundamental frequency picked from the ellipticity curve, to make the different elaborations comparable. The average wavefield contribution was then calculated from the whole set of curves, under the first-order approximation that the *H/V* ratios (and therefore the relative proportion of components) at various sites have similar and comparable shapes, except for the different scaling along the frequency axes. Fig. 6 shows the relative *SH* and *P-SV* contribution over normalized frequency as expressed by eqs (1)–(4). We can note that the frequency peak of the *SH*-wave contribution (f_0-*SH*, maximum of H_{SH}/V_{PSV}, blue line) is higher than the one from *P-SV* (f_0-Ell, maximum of H_{PSV}/V_{PSV}, red line).

To better understand the partition of energy over different frequency bands, we divided the normalized frequency axes into three regions. Below the fundamental frequency f_0-Ell (frequency range A, Fig. 6), the contribution of *SH* and *PSV* waves on the horizontal component is generally comparable. Here, most probably, the energy of surface waves decreases progressively, and the wavefield is controlled by body-wave propagation (Scherbaum *et al.* 2003;
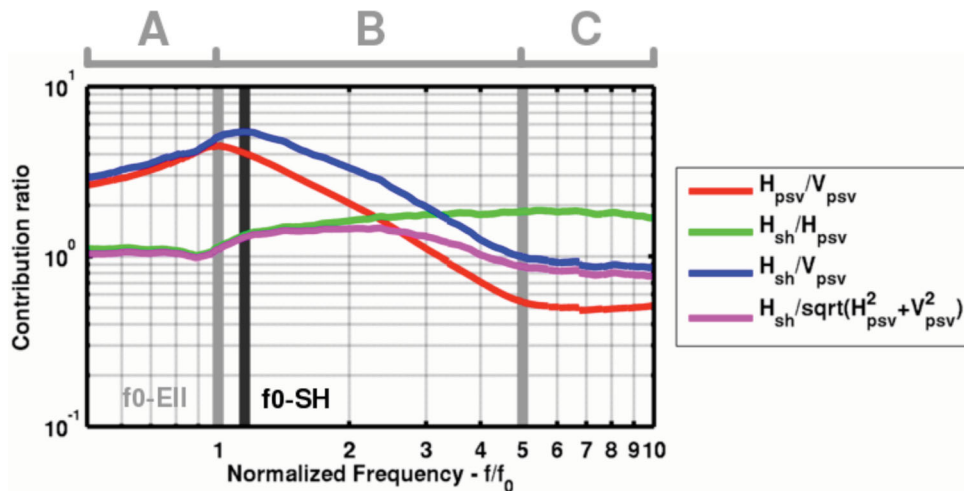

Figure 6. *SH* to *PSV* contribution ratios from the average of all the single station measurements performed in Lucerne. To make the result comparable between different locations, a normalized frequency axes to the *PSV*-fundamental frequency (f_0-Ell) is used.
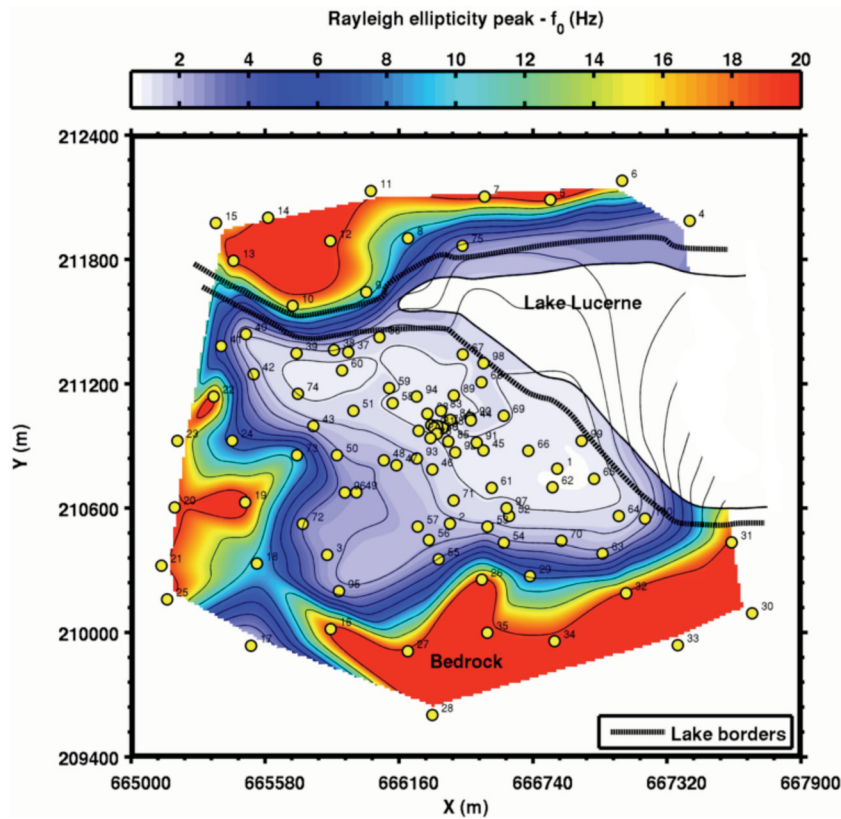
Figure 7. Ellipticity-f_0 (f_0-Ell) map of Lucerne from wavelet-based H/V ratios. Cubic interpolation (in log domain) has been used to map the f_0 over points not directly covered by measurement. The result under the lake, due to the lack of sampling points, must be considered only as interpretational. Units of the map are in Swiss Coordinates (CH1903+).

Albarello & Lunedei 2009). In the middle frequency range (between 1 and 5 Hz, range B, Fig. 6), the SH contribution is dominant on the horizontal component (H_{SH}/H_{PSV}, green line) and Love waves are probably the large contribution among the surface waves. Finally, in the high-frequency range (above 5 Hz, range C, Fig. 6), the contribution of SH and total PSV (including vertical and horizontal, magenta line) is again comparable, but from the inspection of the H_{PSV}/V_{PSV} ratio we can expect Rayleigh waves to be dominant on vertical component.

5.5 Ellipticity f_0 map

It is a common procedure to use the H/V spectral ratios to map the variability of the SH-wave fundamental frequency of resonance over large areas. This parameter is connected with the velocity structure of the basin, and it is consequently used to obtain information about the bedrock depth through simplified approaches (e.g. Hinzen *et al.* 2004). In this work we adopt a different approach, based on the mapping of the Rayleigh-wave ellipticity function as evaluated by wavelet-based H/V spectral ratios. In case of large seismic impedance contrasts between bedrock and sediments, f_0-Ell is close to f_0-SH (e.g. Konno & Omachi 1998; Malischewsky & Scherbaum 2004) but not necessarily coinciding. This might be the case for Lucerne.

The ellipticity function f_0-Ell was manually picked for each processed single station measurement. A quality control was then applied on the H/V spectra, considering the width of the H/V peak, the standard deviation of the curve at this frequency range and the level of noise. Some points were discarded when no clear or unique

peak was identifiable. Some cases needed additional interpretation, especially for those sites close to the basin edges, where the f_0 value is generally at high frequency (roughly >8 Hz). From the ensemble of these values, a map of Rayleigh-wave ellipticity fundamental maximum was then created (Fig. 7). To cover the area where no measurements were available, bicubic interpolation in the log domain has been employed. Additionally, to produce a smoothed representation of the f_0 variability and to minimize the effect of measurement and processing errors, a low-pass filter consisting in a 100×100 m moving average has been applied to the interpolation result.

The distribution of f_0-Ell on the map traces the basin geometry out. The lowest frequency values (<4 Hz) are concentrated in the central part of the basin and correspond to the larger bedrock depths. Due to the presence of the lake, however, it is not possible to assess if lower frequencies can be reached northwest of the city. Here, due to the lack of control points, interpolation results are not realistic and should not be considered for further processing. It is evident from the map that the Lucerne basin is not simply u- or v-shaped, as most alpine valleys, but is characterized by an irregular and asymmetric 3-D geometry, with a side terrace on southwest.

6 ARRAY PROCESSING

6.1 Three-component frequency–wavenumber analysis

Frequency–wavenumber analysis is a technique based on multistation array recording. It is widely used with earthquakes and ambient vibrations recordings to estimate azimuths and apparent phase

velocities of propagating plane waves (e.g. reviews by Tokimatsu 1997; Okada 2003). It is especially suitable for surface wave analysis, because it is possible to retrieve directly the phase-velocity dispersion information. The f–k method (also called beamforming, Lacoss *et al.* 1969) basically implements a sum-and-delay procedure on signals recorded at each station location to induce interference at defined velocities of propagation (VOPs) and directions of arrival (DOAs). Generally a direct grid search over different VOPs and DOAs is performed, until an interference maximum is reached. At this stage the best estimate of the signal properties is detected.

In spite of its simplicity, the major issue of the method concerns its limited resolution capabilities, led by the size, geometry and number of receivers of the array. To partially overcome this limitation, different high-resolution techniques have been proposed with the aim of increasing the resolving power of the array. Data adaptive filters are used to minimize the smearing effect of the array response function, and consequently increase the resolution. This is achieved, however, at the expense of an increased algorithm complexity. One of the most widely used approaches was proposed by Capon (1969), which is usually applied on the vertical component of motion (e.g. Asten & Henstridge 1984). The main disadvantage is the strong sensitivity of the method to the level of uncorrelated noise. Fäh *et al.* (2008) extended this high-resolution technique to the three components of motion, to identify and separate the concurring contributions of Love and Rayleigh waves on the horizontal direction.

Three-component high-resolution f–k analysis has been used to process the data from the SBB array survey in Lucerne. Processing was performed separately for the two concentric ring configurations. To account for statistical uncertainties and the stochastic nature of the ambient vibration wavefield, a signal energy distribution approach (e.g. Wathelet *et al.* 2008; Poggi & Fäh 2010) has been adopted instead of the more common f–k power spectrum representation. In this case, the ambient vibration records were divided in equal time windows of about 2 min. For each window, a complete f–k elaboration was performed and the most energetic signals automatically extracted by relative maxima picking on the power spectrum. In practice, for each window, the three most energetic signals for any given frequency were found. Including an increased number of low-energy maxima would have led to a progressive inclusion of undesired signals artefacts—such as array response side lobes and aliased peaks—and therefore to a more difficult interpretation of the final results. On the other hand, using too few maxima limited the resolution of modes with too low-energy content. From the collection of all picked signals over the consecutive windows, a histogram distribution is built for each separate frequency and a velocity–frequency density map is finally created (e.g. Fig. 8 for inner ring results), which is normalized to the maximum value of the histogram. At first, dispersion curve detection is performed automatically on such a representation through localization of the density distribution modes. Resolution limits for the search are defined as in Poggi & Fäh (2010). Subsequently, the mode identification and separation is manually refined, since a certain level of interpretation is necessary at this stage (Fig. 9, solid coloured lines).

From the analysis of SBB ring 1, we retrieved both Rayleigh- and Love-wave dispersion curves. Regarding the former, the vertical component is well defined in a frequency range between 2 and 8 Hz, while the radial direction gives less resolution, but allows the separation of two modes. By comparing the two directions, it is evident that the vertical component is not composed by a single mode, but from a combination of the fundamental and the first higher modes. In such a case, the Rayleigh-wave energy transfers from one mode to the other at about 3.5 ∼ 4 Hz, where the two curves have an osculation point. Such an interpretation has also been verified by the direct analysis of the signal energy of wavenumber spectral densities (not presented here) for a number of time windows and frequencies. Data from ring 2 recognize very clearly the fundamental and the first higher modes and confirm the interpretation of ring 1. An additional mode is present, but it has not been used during the inversion, because it was not possible to access the mode number. The fundamental mode Love-waves dispersion is retrieved from ring 1 in a frequency range between 2.2 and 4.5 Hz. Ring 2 extends the resolution down to about 1.5 Hz. Some small deviations are clearly notable when comparing the results from the two rings, but they are expected because of the local geology variability under the two configurations.

6.2 Rayleigh ellipticity function from array analysis

In a recent work, Poggi & Fäh (2010) illustrated the use of spectral information retrieved from the three-component f–k transform to obtain an estimation of the Rayleigh-wave ellipticity function. The method relies on the assumption that the amplitude of a maximum in the f–k spectrum is statistically representative of the power amplitude of the picked signal. If three components analysis is performed, the particle motion of each wave contribution can then be evaluated separately. The main advantage of such a procedure is the separation of higher modes, if they are present and sufficiently energetic. The resolution of the f–k method controls the frequency range where such a procedure is effective, which in turn is limited by the array geometry (e.g. the minimum and maximum interstation distances) and the number of receivers. This last, in particular, has the strongest impact on the results.

The results from the analysis of rings 1 and 2 are shown in Fig. 10. In the acceptable frequency range (2.1–8.4 Hz) for the ring 1 configuration, the ellipticity of only one mode is observable, with a clear minimum trough at 5 Hz. According to the interpretation in Fig. 9, the curve should be interpreted as fundamental mode at frequencies higher than about 3.5∼4 Hz, while below this point two different modes should coexist. On the histogram, however, only a moderate increase in the distribution width is observable in this frequency range, but the ellipticity pattern of the two modes cannot be resolved separately. As highlighted by Poggi & Fäh (2010), this is most probably due to the intrinsic limitation of the array method in case of close signals (similar velocities) and with a limited amount of sensors. In such a case, the f–k algorithm is not capable to separate the different energy contributions, providing a unique average result. Most probably, using an increased number of receivers, the ellipticity of the two modes could be better resolved. Therefore, to avoid biased results and misinterpretations, we relied only on the interpretation of the fundamental mode down to about 3.5 Hz. Additionally, a good match is found by comparison of fundamental mode ellipticity pattern from the array method, with that estimated using the wavelet-based approach for all the 14 stations of the SBB array (Fig. 11).

7 VELOCITY MODEL OF THE SEDIMENT BASIN

7.1 Combined inversion of dispersion and ellipticity curves

The joint inversion of the surface wave dispersion and Rayleigh-wave ellipticity curves results in the local velocity structure that
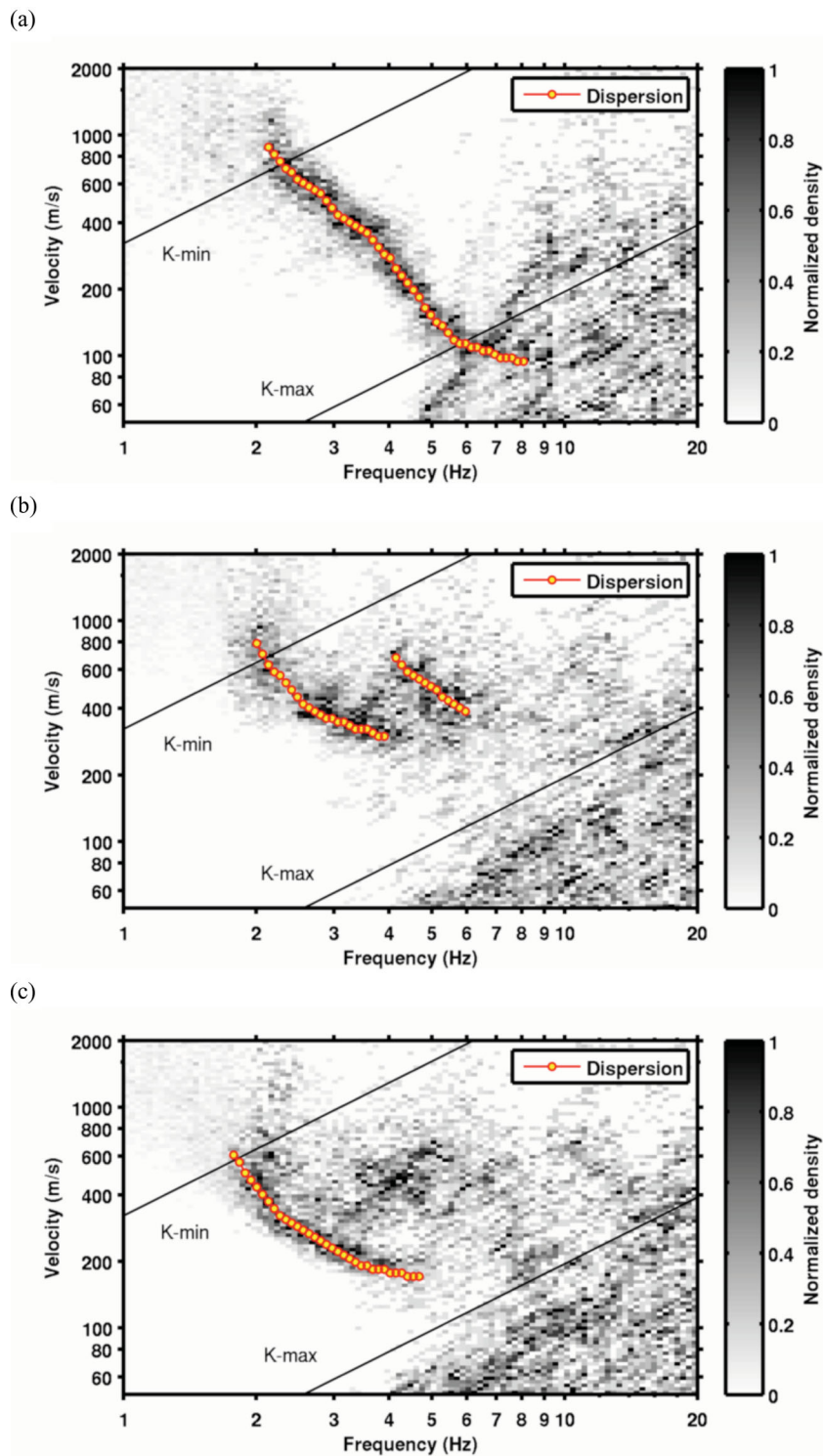
(a)

(b)

(c)

Figure 8. Wavefield decomposition using high-resolution f–k analysis. The contribution of Rayleigh and Love waves can be separated and extracted from the three components of motion. Here an example from the elaboration of the ring 1 of the SBB array. In (a) the vertical, (b) radial and (c) transversal components. Resolution limits of this configuration (K-min, K-max) are also indicated.

better explains a combined set of experimental observations. Several papers (Fäh *et al.* 2003; Hobiger 2011) claim that inverting Rayleigh-wave ellipticity together with surface wave dispersion curves helps in reducing the variability of the inverted models, excluding some solutions incompatible with such a constraint (e.g. Arai & Tokimatsu 2005). As a matter of fact, combining the differ-

ent data sets helped in reducing the scatter (and consequently the uncertainty level) of the final solution.

The inverse problem considered here is highly non-linear and non-unique. Thus, a direct search over the parameter space is a most common optimization method in this case. Constraining the parameter search space by providing some additional *a priori*
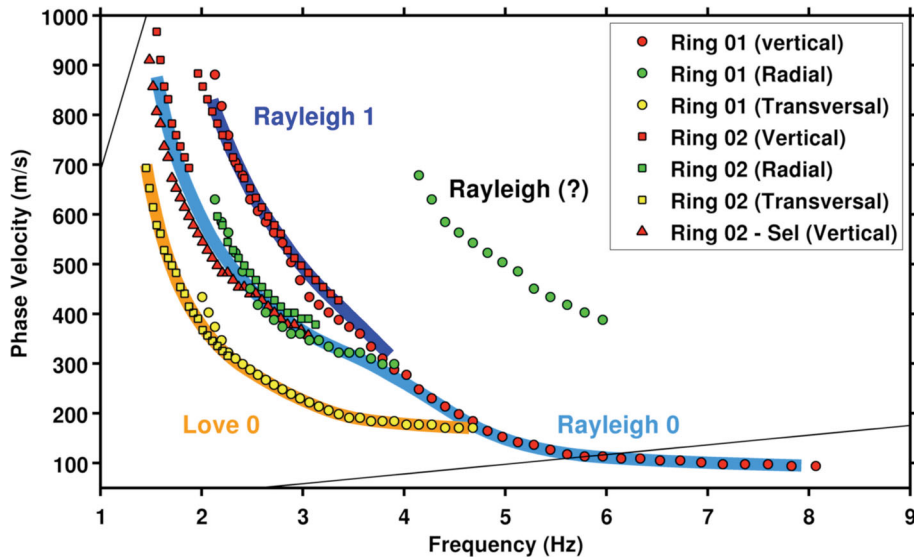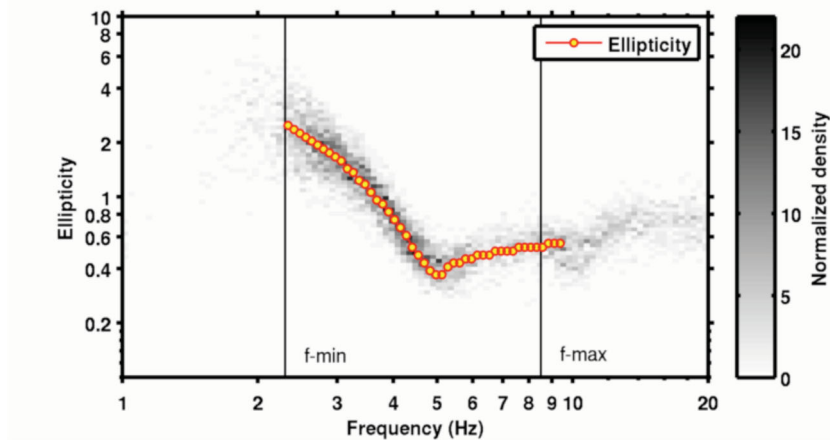
Figure 9. Summary of dispersion information obtained from f–k analysis of the array SBB (ring 1 + ring 2). For Rayleigh waves (on the left), three modes were found. For the third mode, however, mode labelling was not possible. For Love wave (on the right) the fundamental mode only was clearly identifiable. Resolution limits are indicated as black solid lines.
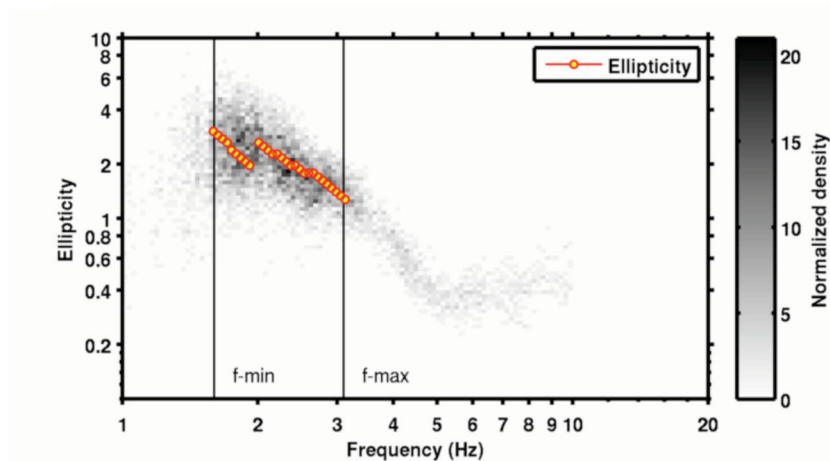
(a)

(b)

Figure 10. Rayleigh-wave ellipticity from three-component array analysis of ambient noise. In (a) the result from ring 1 of the SBB array and in (b) the one from ring 2 is shown. Frequency bounds f-min and f-max are derived from the resolution limits of the f–k method.
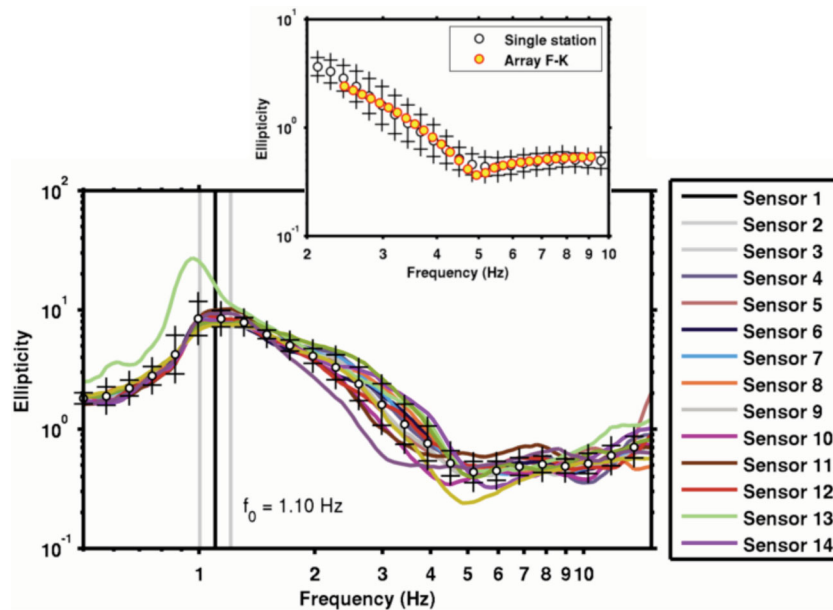
Figure 11. Results from wavelet *H/V* spectral ratio performed on all the 14 stations constituting the SBB array (bottom curves). The average value from all curves is considered as representative of the Rayleigh-wave ellipticity function in this area. A good match is found with results from the array analysis on ring 1 (top box).

information helps in reducing the convergence of the solutions. Each dispersion mode, from both Rayleigh and Love waves, as well as the Rayleigh-wave ellipticity represents a different data set to be fitted. Each data set is usually characterized by a different length (number of data points) and sensitivity to the model parameters. This effect can be overcome by the use of a data-weighting scheme that, on the other side, is generally difficult to quantify. Very often a simple trial-and-error approach is used to define the weights. One dimensionality is a basic assumption for the inversion model. This is generally valid for real structures weak lateral variations. In the case of Lucerne, such approximation is acceptable in most parts of the urban area. In the case of purely elastic models, search parameters are usually V_p, V_s and density of each layer. The sensitivity of dispersion curves to density is however very low (Wathelet *et al.* 2004). For this reason, it is common to prescribe density *a priori*. The number of layers is selected in relation to the expected complexity of the model and the maximum investigated depth.

7.2 The inversion scheme

To invert the experimental curves for the 1-D velocity profiles, a hybrid Monte Carlo optimization scheme was developed. It combines different types of direct search methodologies to drive the inversion to converge to a minimum misfit solution. At first, a pure Monte Carlo search is performed to investigate the whole parameter space. In this stage, about 100 000 models are randomly generated and the best fitting model extracted. Following this, the random search is iterated for a given number of models, progressively refining the search boundaries with respect to the previous best fitting model. In a final stage, the data fit is refined through a Nelder–Mead simplex search approach (Lagarias *et al.* 1998). It is assumed that the *n*-dimensional misfit function is strictly convex in the proximity of the retrieved minimum, where the optimal solution is expected.

Both the Rayleigh- (fundamental and first higher mode) and Love-wave (fundamental) dispersion curves from array analysis were used in the inversion, together with the ellipticity informa-

tion. Love-wave dispersion, in particular, represents a formidable constraint for the shear wave velocity profile. Indirectly, it affects also the *P*-wave characterization during the combined inversion. Actually, both V_s and V_p parameters control Rayleigh-wave dispersion: constraining the first one, the sensitivity of the second will be increased, refining the solution to a narrower parameter space. The frequency range of the curves used for the inversion is controlled mostly by the data availability. An exception is made for the ellipticity function, where we selected the frequency region where the *f–k* and the wavelet methods overlap.

A large number of inversion runs have been performed (about 50 runs with random initial seed), to minimize the risk of solutions trapped in local minima of the misfit function. The two inverted velocity profiles (V_p and V_s) present a smooth increase of the velocity with the depth (Fig. 12). The fit between inverted and original curves is overall good (Fig. 13). Both profiles appear to be reliable down to depths of approximately 120∼140 m. Beyond this value, the dispersion information is progressively incapable to constrain the velocity profile. Thus, there is no constraint on the velocity at the anticipated depth of the interface between soft sediments and the bedrock.

7.3 Generic velocity profiles in gradient form

To characterize the seismic response of the entire sedimentary basin, it is necessary to define a generic velocity model that describes the general variation of the seismic velocity as function of depth. The model should be simple and sufficiently general to be extended over the whole basin structure. As a base for building this generic model, we used the velocity estimates from the inversion of the surface wave dispersion. However, some simplifications were necessary. The inverted profiles, as they are, include some characteristics (sharp velocity jumps on inversion) that are undesirable for a generic model. Therefore, it was decided to simplify the model using a functional form capable to describe the general trend of velocity variation. A gradient equation was then established in the
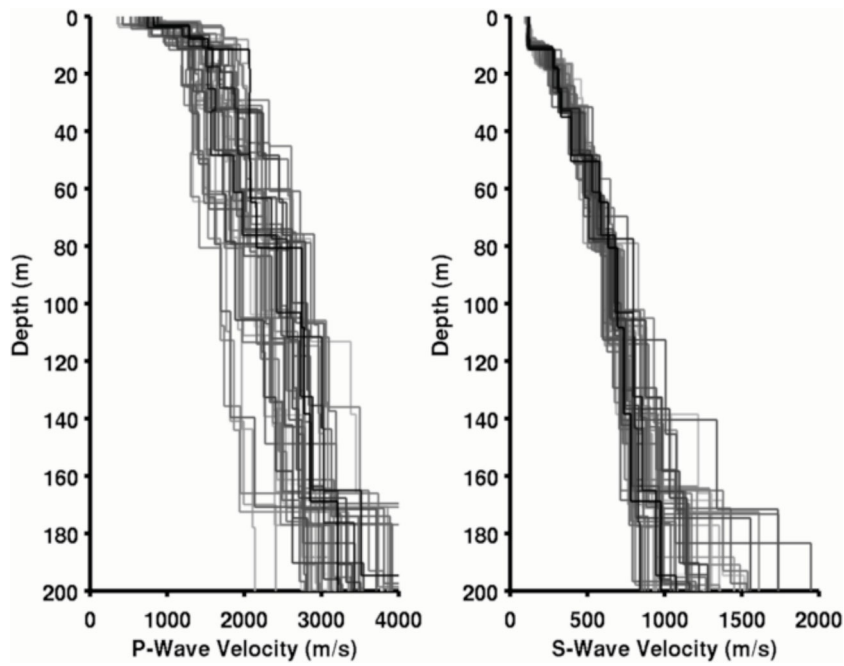
Figure 12. V_s and V_p velocity models from the inversion of surface wave dispersion. The profiles are realistic down to a depth of approximately 120~140 m. Below this depth, the inversion is no more constrained from the available data. In the plot, the best-fitting models of 50 separated runs are shown. It is interesting to note that the velocity jump at about 10–15 m is a common feature.
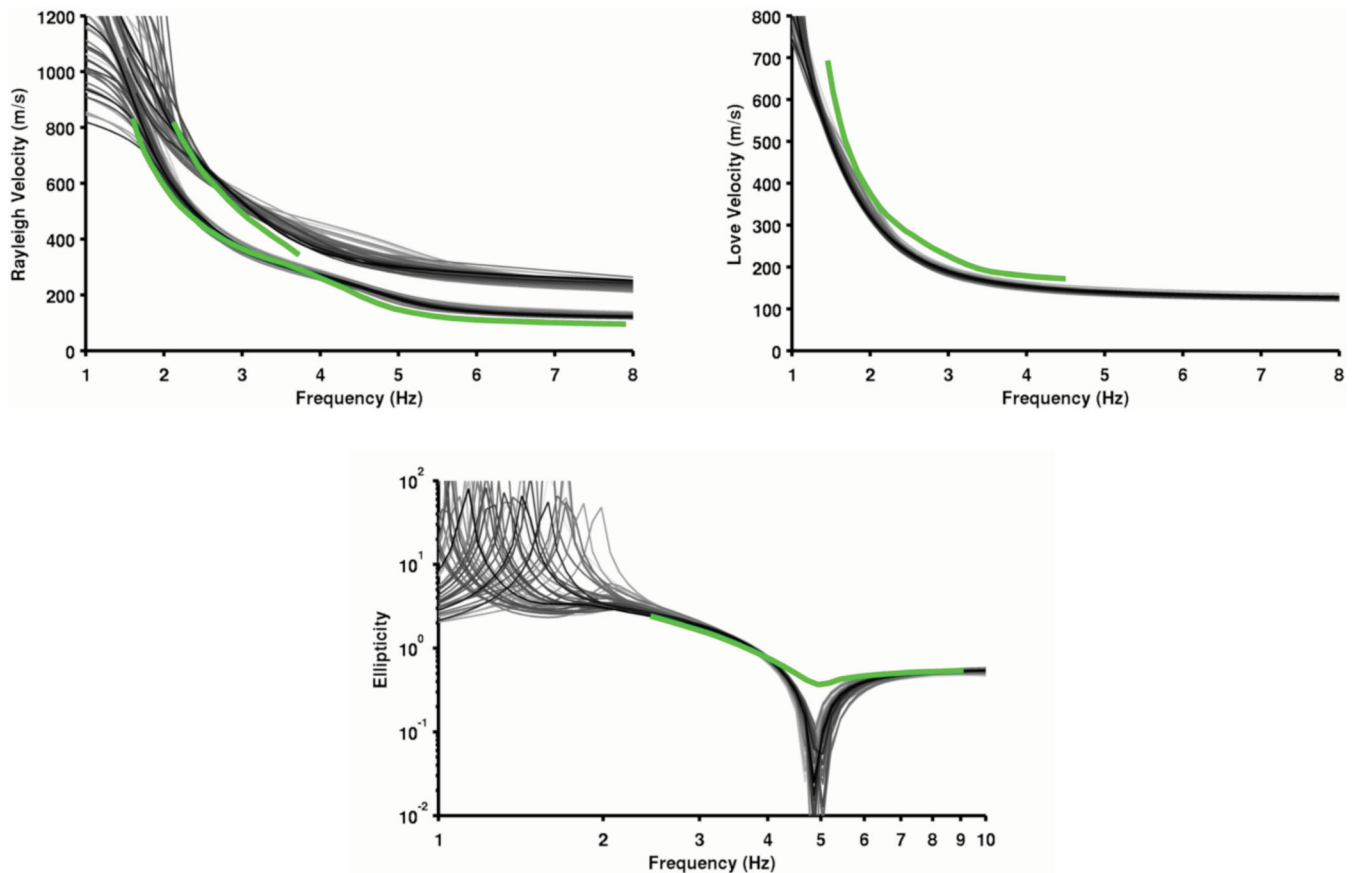

Figure 13. Combined inversion of dispersion and ellipticity information. In green the measured data, in grey the inverted models from the separate 50 runs are shown.
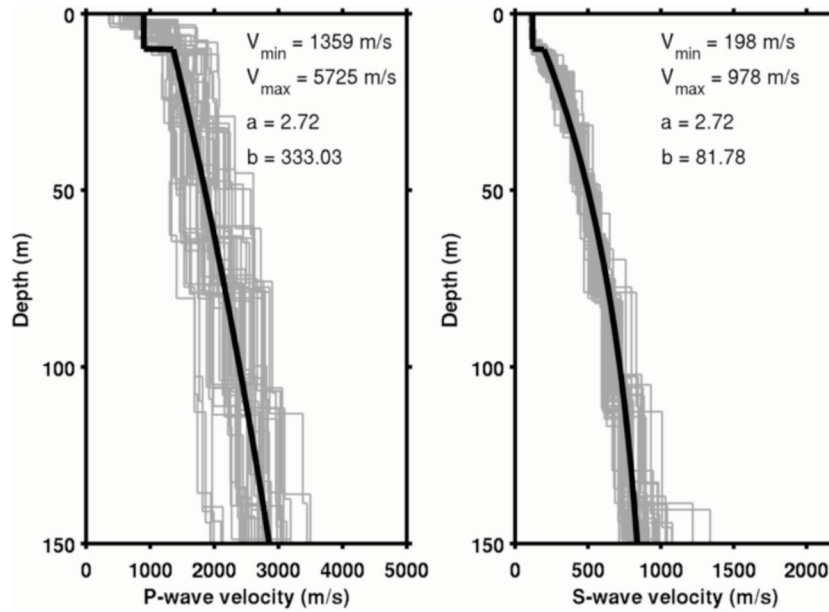
Figure 14. Approximating the inverted V_p (left-hand side) and V_s (right-hand side) velocity profile by mean of a simplified gradient function (black line). The fit is obtained through a global optimization procedure, accounting also for the consistency with the dispersion and ellipticity data.

form (Poggi *et al.* 2011):

$$V(z) = (V_{max} - V_{min})\left[1 - a^{\left(\frac{z_0 - z}{b}\right)}\right] + V_{min}, \tag{5}$$

where V_{max} and V_{min} are, respectively, the expected maximum and minimum velocities, while a and b are curvature coefficients. Note that in this way, the shallower low-velocity layer is then modelled by mean of a single layer of constant velocity (V_{min}) and 10 m thickness (z_0). Two set of coefficients, as well as maximum and minimum velocities, were established to model *P*- and *S*-wave velocity profiles separately.

Fitting between the gradient function (5) and the inverted velocity models is done through a simple optimization procedure. Free parameters for the search are the velocity bounds and the curvature coefficients of the function. The optimal model minimizes the velocity residuals between the input profile and the gradient in a depth range between 0.5 and 200 m. In Fig. 14 the V_p and V_s gradient velocity profiles obtained with such a procedure are presented. The selected gradient functions have a reasonable fit also with the observed dispersion and ellipticity curves (not presented here).

8 MAPPING THE BEDROCK DEPTH

8.1 Global inversion of ellipticity peaks

Combined inversion of the ellipticity function and dispersion characteristics improves the resolution of the bedrock for simple models with few layers over a half-space. In more complex models, however, and with an increasing number of layers, the inversion often results in a smoothed profile, where the bedrock interface is not clearly identifiable (Fäh *et al.* 2009). To face such a drawback, we adopted a two-step inversion approach. In a first step, a gradient velocity model (in terms of V_p and V_s) was established for the soft sediment part. Because of the limited size of the basin, similar depositional conditions and geological settings are expected over the whole area. For this reason it appears reasonable to assume the retrieved velocity model as representative of the basin. Clearly, local

variations might be present (e.g. lateral variations), but these are assumed to be in the order of the error of the method. Under this assumption, the only variable and unknown parameter is therefore the bedrock depth under the basin. In a second stage, then, the singularity or peak of the ellipticity function (f_0-Ell) from wavelet H/V ratios is used, together with the derived generic gradient model, to constrain the bedrock depth at each measuring location.

By keeping the velocity model for the sediment part constant, the bedrock depth is varied till a good match is found between the observed and computed f_0-Ell. The shear wave velocity of the bedrock is imposed to be constant 2200 m s^{-1}. This value was derived from a previous study performed on the area (Mengis & Lorenz AG 2007, unpublished data). To constraint the V_p of the bedrock, we used a constant Poisson ratio of 0.3, which appears a reasonable estimate for compact clastic rocks. The described procedure was then iterated over a subset of single station measurements, selected within parts of the sedimentary basin where stable estimates of f_0-Ell from wavelet H/V are expected. The selection was then done by setting an approximate upper bound for the ellipticity f_0-Ell values of about 4 Hz. For all these stations, a value for the bedrock depth was derived (see e.g. depth estimate for the SBB area in Fig. 15). Close to the basin edges (f_0-Ell above 4 Hz), a certain amount of scattering is observed in the ellipticity peak, which is probably due to 2-D/3-D effects.

As proposed by Parolai *et al.* (2002) for f_0-SH, a functional correlation between inverted depths and the corresponding ellipticity f_0-Ell was established (Fig. 16). The relation is exponential and expresses as follows:

$$Z_{Bedrock} = 158.54 \left(f_0^{Ell}\right)^{-2.45}. \tag{6}$$

The use of relation (6) allows the rapid inversion of the bedrock depth in those areas for which an estimation of the ellipticity f_0-Ell is available, without the necessity of an inversion approach. Relation (6) has then been used to convert the smoothed f_0-Ell map of Fig. 7 into the corresponding bedrock map (Fig. 17). We do not expect the correlation to be strictly valid at high frequencies. Therefore, portions of the f_0-Ell map with frequencies above 10 Hz were
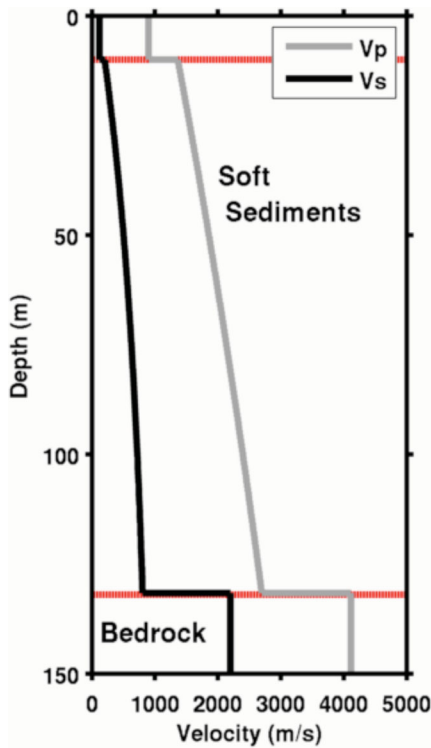
Figure 15. Inverting the bedrock depth and velocity for the SBB array from wavelet-based *H/V* ratios (assuming that we measured ellipticity). Inverted depth is in agreement with interpretations from previous geophysical surveys (Mengis & Lorenz 2007a).
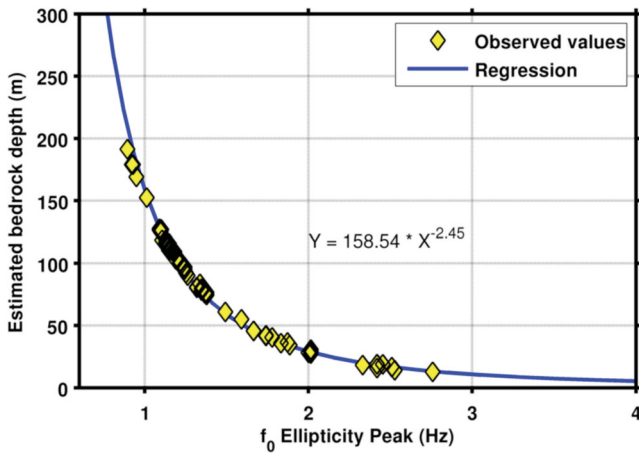

Figure 16. Globally inverting the ellipticity peaks (f_0-Ell) from wavelet-based *H/V* ratios helps in minimizing the uncertainties introduced by the inversion procedure. An exponential regression is used to describe the relation between the frequency value and inverted depth.

considered cropping out bedrock (Fig. 17, in grey). The retrieved bedrock geometry reflects the distribution of f_0-Ell along the area. The largest depth obtained from the correlation is 212 m in the southeastern part of the basin. The central area of the basin has variable thickness, with an average value of about 120∼150 m. Bedrock depth is clearly decreasing while approaching the basin edges (e.g. profiles A-B and C-D in Fig. 17).

8.2 Comparison with the simplified *SH*-resonance approach

A common approach to estimate the bedrock depth from *H/V* spectral ratios is to assume the peak of the ellipticity function to be a proxy for the *SH*-wave fundamental frequency of resonance (Yamanaka *et al.* 1994; Hinzen *et al.* 2004). In such a way, if the velocity model is simplified to a 1-D case of a single soft-sediment layer over the bedrock half-space, the following equation is valid (Roesset 1970):

$$f_0^{SH} = \frac{Vs_{\mathrm{Soft}}}{4 \cdot z_{\mathrm{Bedrock}}}. \tag{7}$$

This equation relates the *SH*-wave fundamental frequency of resonance f_0-*SH* with the V_s velocity of the equivalent layer and the bedrock depth z_{Bedrock}. Such an approach, however, often results in an oversimplification of the problem (Dobry *et al.* 1976). In particular, the choice of the proper 'average' V_s velocity is not straightforward. In most cases, shear wave velocity is estimated at shallower depths only (e.g. 30 m) from geotechnical characterization or small-scale geophysical surveys, and then assumed to be constant down to bedrock. This approach systematically underestimates the velocities of basins having thick sedimentary cover, resulting in an underestimation of the bedrock depth.

To underline the entity of such deviations, bedrock depths obtained by the proposed method have been compared with those from the simplified approach (Fig. 18). Different V_s velocities were used for the test, averaging the available velocity profile at the depths of 10, 30 50, 100 and 200 m. As expected, large differences are present. In particular, if compared with our reference array location, for which the bedrock depth is estimated to be about 130 m, the common V_s^{30} averaging (common in engineering applications) produces a significant underestimation of depth. The error decreases while increasing the averaging depth, but always results in an error.

9 FREQUENCY-DEPENDENT AMPLIFICATION MODEL

9.1 Pseudo-3-D modelling of amplification

In this section we show the frequency-dependent *S*-wave amplification map of Lucerne, computed using the 3-D model derived from ambient vibration techniques. Considering the uncertainties of the model and the assumptions, it was decided to avoid any 2-D/3-D wave-propagation simulation for the computation. The level of knowledge of the model is not yet sufficient, specifically lacking the information related to the variability of the shallow low-velocity layer in the first 10–15 m.

A robust, nevertheless simple, approach was instead used: a gridded 1-D modelling. This approach consists in subdividing the 3-D model in vertical soil columns. The basin area has been discretized in the horizontal plane using a grid of 100 × 100 cells of about 25 m resolution. For each of these, a 1-D modelling of the *SH*-wave amplification is done. This strategy is generally valid in cases of moderate variation of the elastic and geometric properties of the model. Since 2-D resonance patterns involve both vertical and horizontal interferences, they can only appear in relatively deep valleys. To identify valleys whose seismic behaviour is characterized by 2-D resonance, Bard & Bouchon (1985) introduced the concept of the 'critical shape ratio'. Considering the structural characteristics of the basin, Lucerne is clearly located outside in the domain of 2-D resonance for the *SH*-case. However, basin edge effects might
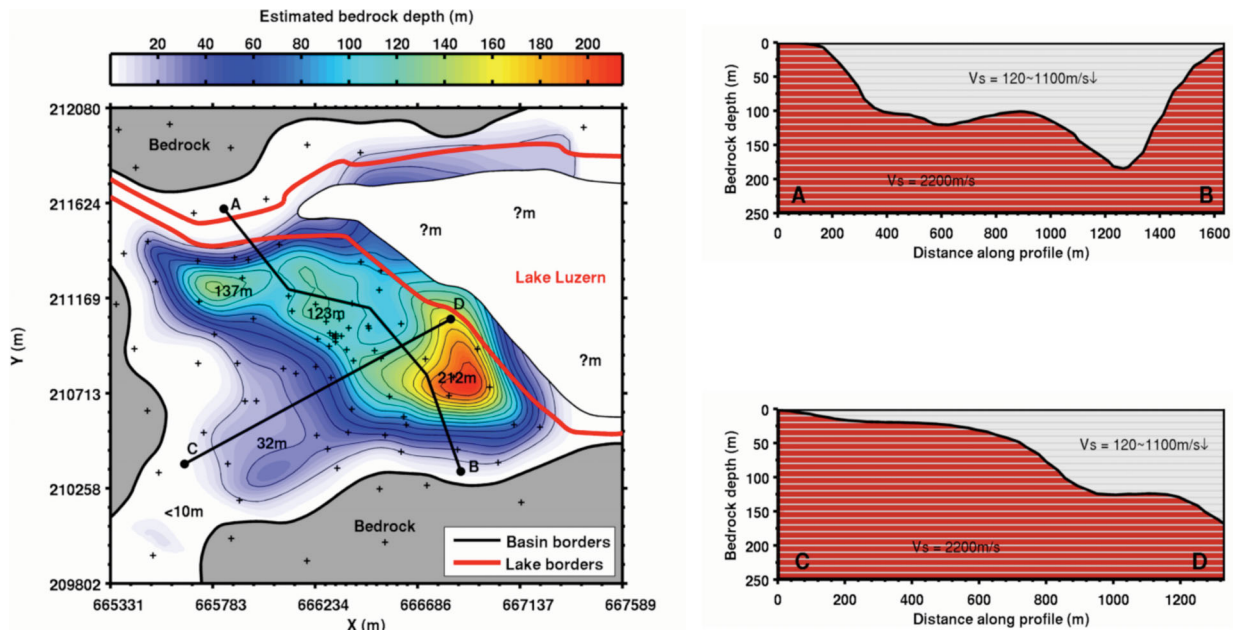
Figure 17. The functional correlation between ellipticity peak and inverted bedrock depth allows the reconstruction of the bedrock geometry, from the interpolated f_0-Ell map.
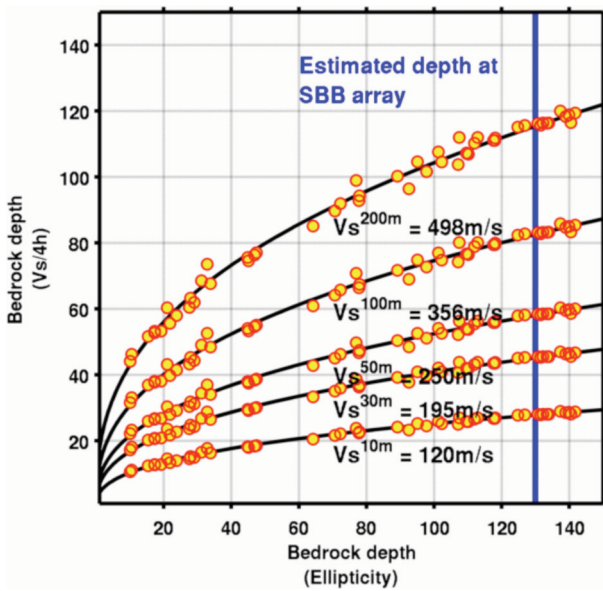

Figure 18. Bedrock depths estimated using the ellipticity peak have been compared with those obtained from the simple equation $f_0 = V_s/4h$ assuming a layer over half-space. Different average velocities were used for the comparison, averaging velocity over the depths 10 m, 30 m, 50 m, 100 m and 200 m. For the site of the SBB array, the results of this simplified method always underestimate the one from the proposed one. The correct bedrock depth of 130 m at the location of seismic survey cannot be retrieved with such an oversimplified approach. Black lines are lognormal regressions to underline the trend of each set.

still play a major role in some Lucerne areas, and they cannot be modelled by 1-D site response.

9.2 Using the *SH*-wave transfer function

To compute the 1-D amplification function at each cell, we used the *SH*-wave transfer function for vertical wave propagation, fol-

lowing the Knopoff layer-matrix formulation (Knopoff 1964). The constant bedrock velocity of 2200 m s^{-1} and density of 2500 kg m^{-3} are assumed as reference. No information about anelastic attenuation is available from the ambient vibration analysis. Therefore, for the sediment part we propose dependency between V_s and Qs. Such profile varies between $Qs = 10$, in the shallow layers, and 30 at 150 m. For the bedrock, a constant Qs value of 50 was used. Amplification functions were computed in the 0.5–15 Hz frequency range.

The simple 1-D modelling shows interesting results (Fig. 19). From low to high frequencies, it is possible to follow the development of the fundamental mode of resonance, progressively moving from the basin centre to the edges. Higher modes of resonance are also developed. Mapping the maximum amplification at the fundamental frequency of resonance f_0-*SH* shows that the highest amplification (about 9) is found in the southwestern part of the basin (Fig. 20), where the bedrock depth is estimated to be between about 30 and 60 m. Large parts of the basin show amplifications between a factor of 6 and 7. These values of amplification depend strongly on the sediment-bedrock velocity jump of the adopted model. The amplification at higher frequencies is depending on the Q model. Only earthquake observations can help to better define these uncertainties.

9.3 Comparing the measured ellipticity peak to computed f_0-*SH*

The map of the ellipticity fundamental frequency from wavelet analysis is now compared with the variation in the *SH*-wave fundamental frequency (Fig. 21a). Away from the basin edges, it is possible to observe a generally good match between them. The strong differences at the borders can be justified by the limitations of the proposed method, where the 1-D approximation (for the ellipticity inversion and transfer function modelling) might not be fulfilled, and measured f_0-Ell are affected by edge effects. For this reason, we decided to define an f_0 value of 4 Hz value as a limit to separate the more reliable part of the model. This roughly corresponds to a bedrock depth of about 20 m.
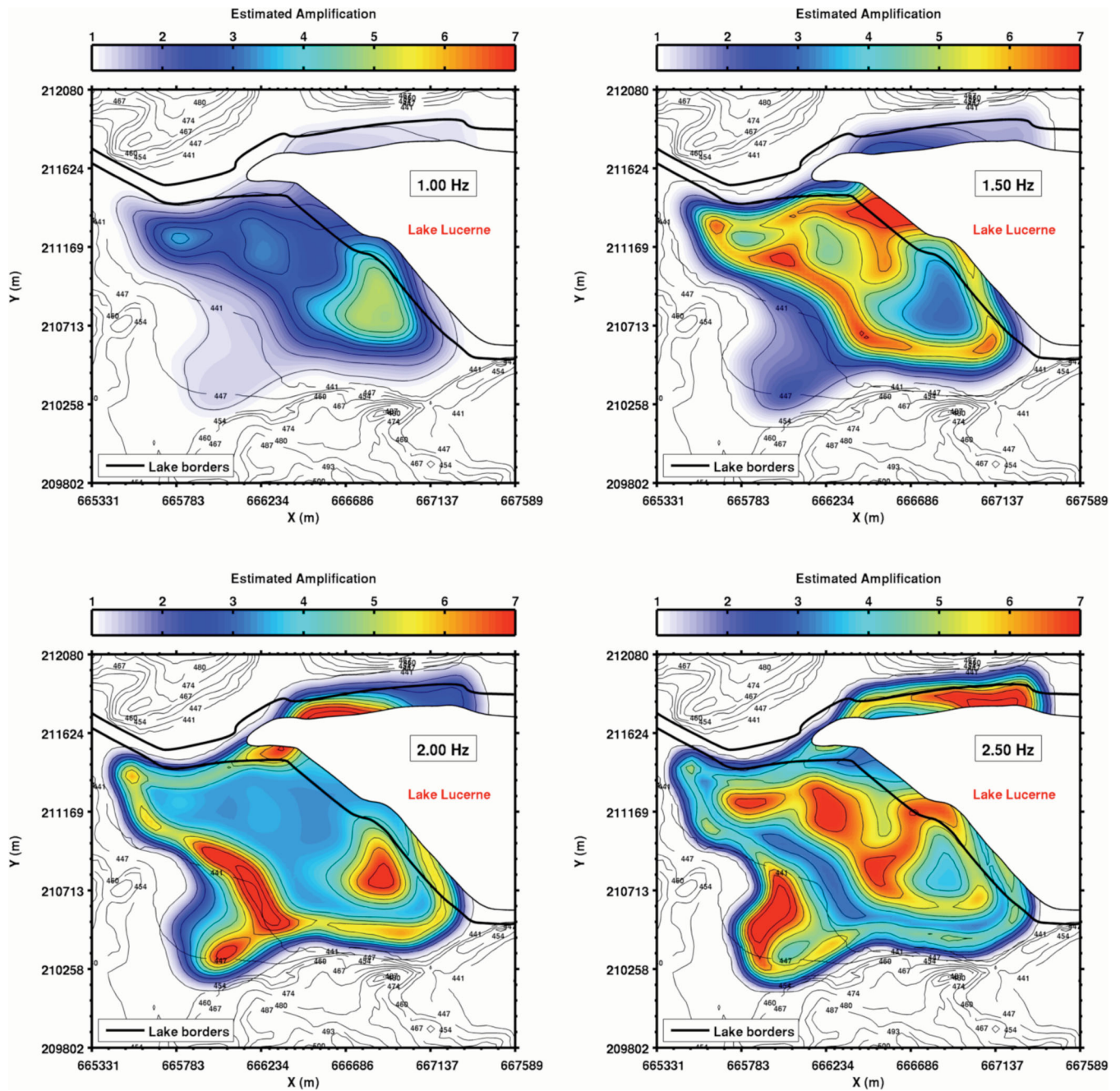
Figure 19. *SH*-wave transfer function amplification model of the Lucerne basin using a gridded pseudo-3-D approach. Here some frequency snapshots from 1 to 2.5 Hz are shown. It is clearly possible to observe the migration of the first two resonance modes from the centre to the basin edges with increasing frequencies.

Comparing more accurately the two frequency parameters (Figs 21b and c) in a range between 1 and 4 Hz, some small local deviations can still be observed. In particular, the *SH*-wave f_0 tends to be slightly (but consistently) larger than that from ellipticity in a range between 1 and 3 Hz. This is generally in agreement with what already was observed in Fig. 8 by comparing different *H/V* spectral ratio methods. This provides also a further confirmation of the imperfect equivalence between f_0 from ellipticity (or better the singularity of the ellipticity curve) and f_0 from the *SH* transfer function. As outlined by Malischewky & Scherbaum (2004) these two parameters, often considered equivalent in literature, belong to different phenomena and might consequently show some deviations.

Nevertheless this is not relevant for a practical application, because such deviations are usually within the range of uncertainties of the methods.

10 CONCLUSIONS

In this study we deal with the problem of optimizing the characterization and subsequent use of the Rayleigh-wave ellipticity information from ambient noise recordings. The main goal is to improve the level of accuracy in assessing the velocity structure of sedimentary basins, with special regard to the bedrock depth. As a direct consequence, the uncertainty in the local amplification model can be reduced.
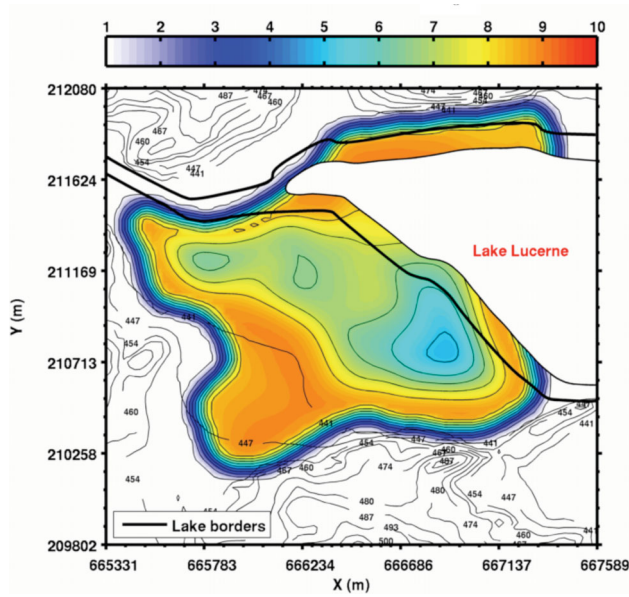
Figure 20. Amplitude map of the first *SH* resonance in the study area. Maximum amplification is experienced where the bedrock depth is roughly between 30 and 60 m.

Two new techniques to evaluate the Rayleigh ellipticity were tested, a single station method and an array method. The two approaches provide comparable results in the limit of resolution of the methods. Ellipticity information obtained in this way can be used

as an additional constraint to invert for the velocity structure. The use of wavelet time–frequency analysis to perform *H/V* polarization analysis has the clear advantage of minimizing the effect of *SH*-wave contribution, compared to the classical *H/V* method. In case of large velocity contrast between sediments and bedrock, the result can be reasonably considered representative of the Rayleigh-wave ellipticity function. Additionally, by comparing the classic and the wavelet-based method to compute *H/V* ratios, it is possible to estimate the relative energy contribution between the *SH* and *PSV* components. The method, however, is not capable to separate the contribution from different modes. Estimating the Rayleigh-wave ellipticity function by means of array analysis provided comparable results with respect to those obtained from wavelet approach. The main disadvantage, however, is the limited resolution of the method. This strictly depends on the number of sensors employed for the surveys and the array geometry. In this case, the 14 receivers employed are sufficient to estimate a portion of the fundamental mode ellipticity, but not optimal to separate the contribution of higher modes. To improve the final result, therefore, we recommend an increased number of receivers.

A two-step approach was introduced for the combined use of dispersion and ellipticity information from ambient noise recordings. Such an approach enhances the resolution of classical array techniques on deep structures, especially on the depth of the bedrock. This is particularly suitable in densely populated areas, where more sophisticated techniques are generally difficult or even impossible (e.g. active source seismic). Moreover, it is cost effective, which makes it suitable for investigations over large areas. Uncertainties, affecting the quality of the 3-D structural model and therefore
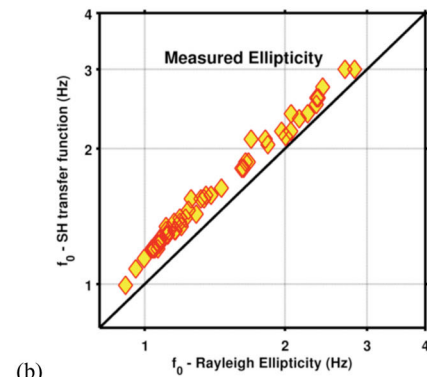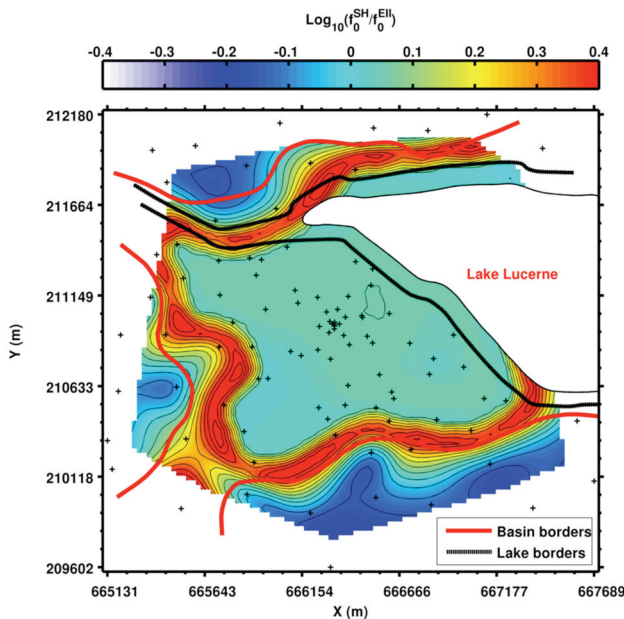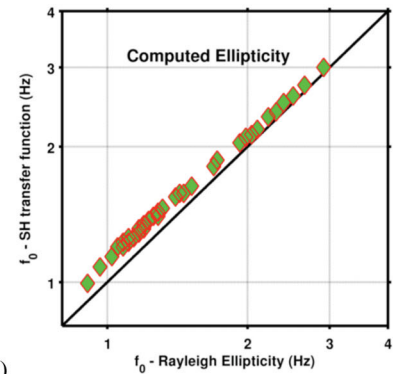
Figure 21. Comparison between ellipticity f_0-Ell from single station measurements and computed *SH*-wave fundamental frequency of resonance for the basin area (a). Strong deviations are experienced close to the basin edges, where the ellipticity f_0 is usually higher than 4 Hz. Below 4 Hz, deviations are less pronounced, and only a slight overestimation of the f_0-*SH* can be observed (b,c). In (b) theoretical f_0-*SH* are compared to the observed f_0-Ell, and in (c) theoretical f_0-*SH* are compared to the theoretical f_0-Ell at the site of the measurements.

the estimated amplification, are the local variability in the velocity structure (e.g. in the uppermost low-velocity layer in the Lucerne area), the influence of 2-D/3-D effects at the basin edges and the uncertainties in attenuation. In particular, estimation of confidence bounds for the inverted velocity profiles has to be defined by further independent measurements.

The evaluation of the local seismic response has been carried out from the inverted velocity model using the 1-D approximation. The amplification functions have been calculated using the *SH*-wave transfer function approach. Consequently, the modes of 1-D vibration can be tracked along the basin at different frequencies. The latter gives explanation of the amplification induced by the velocity contrast between the bedrock and soft sediments only. Effects such as basin edge effects or 3-D resonances might play a major role in some areas of Lucerne, and are not properly modelled by 1-D site response. Further studies will focus on improving the knowledge of the variable surface layer, and on numerical 3-D wave-propagation modelling. Two permanent strong motion sensors are presently installed in Lucerne that will further help us to improve the structural model. In dealing with strong motion events, non-linear behaviour of the soils is expected, which needs further geotechnical measurements and techniques that will allow us to model non-linear phenomena.

ACKNOWLEDGMENTS

REFERENCES

Albarello, D. & Lunedei, E., 2009. Alternative interpretations of horizontal to vertical spectral ratios of ambient vibrations: new insights from theoretical modelling. *Bull. Earthq. Eng.*, **8**, 519–534, doi:10.1007/s10518-009-9110-0.

Arai, H. & Tokimatsu, K., 2005. S-wave velocity profiling by joint inversion of microtremor dispersion curve and horizontal-tovertical (H/V) spectrum. *Bull. seism. Soc. Am.*, **95**(5), 1766–1778.

Arai, H. & Tokimatsu, K., 2008. Three-dimensional V-S profiling using microtremors in Kushiro, Japan. *Earthq. Eng. Struct. Dyn.*, **37**, 845–859.

Asten, M.-W. & Henstridge, J.-D., 1984. Array estimators and the use of microseisms for reconnaissance of sedimentary basins, *Geophysics*, **49**, 1828–1837.

Asten, M., Stephenson, W. & Davenport, N., 2005. Shear-wave velocity profile for holocene sediments measured from microtremor array studies, SCPT, and seismic refraction, *J. Eng. Environ. Geophys.*, **10**, 235–242.

Bard, P.-Y. & Bouchon, M., 1985. The two-dimensional resonance of sediment-filled valleys, *Bull. seism. Soc. Am.*, **75**(2), 519–541.

Bard, P.-Y., Jongmans, D., Ohrnberger, M. & Wathelet, M., 2005. Recommendations for quality array measurements and processing, SESAME deliverable D24.13.

Basler & Partner, 2007. Sicherheitsbericht für die Stadt Luzern. Stadt Luzern, Sicherheitsdirektion.

Bonnefoy-Claudet, S., Cornou, C., Bard, P.-Y., Cotton, F., Moczo, P., Kristek, J. & D. Fäh, 2006a. H/V ratio: a tool for site effects evaluation. Results from 1D noise simulations. *Geophys. J. Int.*, **167**, 827–837.

Bonnefoy-Claudet, S., Cotton, F. & Bard, P.-Y., 2006b. The nature of noise wavefield and its applications for site effects studies. A literature review. *Earth-Sci. Rev.*, **79**, 205–227.

Bonnefoy-Claudet, S., Köhler, A., Cornou, C., Wathelet, M. & Bard, P.-Y., 2008. Effects of Love waves on microtremor H/V ratio, *Bull. seism. Soc. Am.*, **98**, 288–300.

Capon, J., 1969. High resolution frequency wavenumber spectrum analysis, *Proc. IEEE*, **57**, 1408–1418.

CEN, European Committee for Standardization (2004). Eurocode 8: design of structures for earthquake resistance—part 1: general rules, seismic actions and rules for buildings. Bruxelles.

Chavez-Garcia, F.J., Sanchez, L.R. & Hatzfeld,D., 1996. Topographic site effects and HVSR. A comparison between observations and theory. *Bull. seism. Soc. Am.*, **86–5,** 1559–1573.

Dobry, R., Oweis, I. & Urzua, A., 1976. Simplified procedures for estimating the fundamental period of a soil profile, *Bull. seism. Soc. Am.*, **66**, 1293–1321.

Endrun, B., 2010. Love wave contribution to the ambient vibration H/V amplitude peak observed with arrray measurements. *J. Seismol.*, **15**, 443–472, doi:10.1007/s10950-010-9191-x.

Fäh, D., Kind, F. & Giardini,D., 2001. A theoretical investigation of average H/V ratios. *Geophys. J. Int.*, **145**, 535–549.

Fäh, D., Kind, F. & Giardini, D., 2003. Inversion of local S-wave velocity structures from average H/V ratios, and their use for the estimation of site-effects. *J. Seismol.*, **7**, 449–467.

Fäh, D., Stamm, G. & Havenith, H.-B., 2008. Analysis of three-component ambient vibration array measurements, *Geophys. J. Int.*, **172**, 199–213.

Fäh, D. *et al*., 2009. Using ellipticity information for site characterisation, NERIES JRA4 "Geotechnical Site Characterization", taskB2-D4, final report.

Gisler, M., Fäh, D. & Kästli, P., 2004. Historical seismicity in central Switzerland, *Eclogae Geol. Helv.*, **97**, 221–236.

Goupillaud, P., Grossman, A. & Morlet, J., 1984. Cycle-octave and related transforms in seismic signal analysis, *Geoexploration*, **23**, 85–102.

Haghshenas, E., Bard, P.-Y., Theodulidis, N. & SESAME WP04 Team, 2008. Empirical evaluation of microtremor H/V spectral ratio, *Bull. Earthq. Eng.* **6**(1), 75–108.

Hinzen, K.G., Weber, B. & Scherbaum, F., 2004. On the resolution of H/V measurements to determine sediment thickness, a case study across a normal fault in the lower Rhine embayment, Germany. *J. Earthq. Eng.,* **8**(6), 909–926.

Hobiger, M, 2011. Polarization of surface waves: characterization, inversion and application to seismic hazard assessment, *PhD thesis*. Institut des Sciences de la Terre (ISTerre), Grenoble, France.

Horike, M., 1985. Inversion of phase velocity of long-period microtremors to the S-wave-velocity structure down to the basement in urbanized areas, *J. Phys. Earth*, **33**, 59–96.

Jongmans, D., Ohrnberger, M. & Wathelet, M., 2005. Recommendations for quality array measurements and processing. Final Report of the SESAME Project, WP13.

Knopoff, L., 1964. A matrix method for elastic wave problems, *Bull. seism. Soc. Am.*, **54**, 431–438.

Konno, K. & Omachi T. 1998. Ground motion characteristics estimated from spectral ratio between horizontal and vertical components of microtremors, *Bull. seism. Soc. Am.*, **88**, 228–241.

Kristekova, M., 2006. Time-frequency analysis of seismic signals, *PhD thesis*. Slovak Academy of Sciences, Bratislava, Slovakia.

Lachet, C., Hatzfeld, D., Bard, P.-Y., Theodulidis, N., Papaioannou, C. & Savvaidis, A., 1996. Site effects and microzonation in the city of Thessaloniki (Greece): comparison of different aproaches, *Bull. seism. Soc. Am.*, **86,** 1692–1703.

Lacoss, R.-T., Kelly, E.-J. & Toksz, M.-N., 1969. Estimation of seismic noise structure using arrays, *Geophysics,* **34,** 21–38.

Lagarias, J.C., Reeds, J. A., Wright, M. H. & Wright, P. E., 1998. Convergence properties of the Nelder-Mead simplex method in low dimensions, *SIAM J. Optim.,* **9**(1), 112–147.

Lermo, J. & Chavez-Garcıa, F.J., 1994. Are microtremors useful in site response evaluation? *Bull. seism. Soc. Am.,* **84,** 1350–1364.

Malischewsky, P.G. & Scherbaum,F., 2004. Love's formula and H/V-ratio (ellipticity) of Rayleigh waves, *Wave Motion,* **40,** 57–67.

Nakamura, Y., 1989. A method for dynamic characteristics estimation of subsurface using microtremor on the ground surface, Rep. *Railway Tech. Res. Inst.*, Jpn 30, **1,** 2533.

Okada, H., 2003. *The Microseismic Survey Method,* Society of Exploration Geophysicists of Japan, Translated by Koya Suto, Geophysical Monograph Series, No. 12, Society of Exploration Geophysicists, Tulsa.

Parolai, S., Bormann, P. & Milkereit, C., 2002. New relationships between Vs, thickness of sediments, and resonance frequency calculated by the H/V ratio of seismic noise for the Cologne Area (Germany), *Bull. seism. Soc. Am.,* **92**(6), 2521–2527.

Poggi, V. & Fäh D., 2010. Estimating Rayleigh wave particle motion from three-component array analysis of ambient vibrations, *Geophys. J. Int.,* **180–1,** 251–267.

Poggi, V., Edwards, B. & Fäh D., 2011. Derivation of a reference shear-wave velocity model from empirical site amplification, *Bull. seism. Soc. Am.,* **101,** 258–274, doi:10.1785/0120100060.

Roesset, J. M., 1970. Fundamentals of soil amplification, in *Seismic Design for Nuclear Power Plants,* pp. 183–244, ed. Hansen, R.J., M.I.T. Press, Cambridge, MA.

Scherbaum, F., Hinzen, K. G. & Ohrnberger, M., 2003. Determination of shallow shear wave velocity profiles in the Cologne Germany area using ambient vibrations, *Geophys. J. Int.,* **152,** 597–612.

Schwarz-Zanetti, G., Fäh, D., Schibler, R., Masciadri, V. Kästli, P. & Giardini, D., 2003. The earthquake in Unterwalden and the rockslide from the Bürgenstock into Lake Lucerne on September 18, 1601. *Eclogae geol. Helv.,* **96,** 441–450.

SIA, 2003. Actions on Structures, SIA261:2003. SN 505 261. Swiss Standards, Swiss Society of Engineers and Architects.

Strasser, M., Anselmetti, F., Fäh, D., Giardini, D. & Schnellmann, M., 2006. Magnitudes and source areas of large prehistoric northern Alpine earthquakes revealed by slope failures in lakes. *Geology,* **34**(12), 1005–1008, doi:10.1130/G22784A.1.

Theodulidis, N., Bard, P.-Y., Archuleta R.J & Bouchon, M., 1996. Horizontal to vertical spectral ratio and geological conditions: the case of Garner Valley downhole array in Southern California, *Bull. seism. Soc. Am.,* **86,** 306–319.

Tokimatsu, K., 1997. Geotechnical site characterization using surface waves, in *Proceedings of the 1st International Conference of Earthquake Geotechnical Engineering,* ed. Ishihara, K., Balkema, Rotterdam, the Netherlands, pp. 1333–1368.

Wathelet, M., Jongmans, D. & Ohrnberger, M., 2004. Surface wave inversion using a direct search algorithm and its application to ambient vibration measurements, *Near Surf. Geophys.,* **2,** 211–221.

Wathelet, M., Jongmans, D., Ohrnberger, M. & Bonnefoy-Claudet S., 2008. Array performances for ambient vibrations on a shallow structure and consequences over Vs inversion, *J. Seismol.,* **12,** 1–19.

Yamanaka, H., Takemura, M., Ishida, H. & Niwa, M., 1994. Characteristics of long-period microtremors and their applicability in exploration of deep sedimentary layers. *Bull. seism. Soc. Am.,* **84**(6), 1831–1841.